

# Phase Retrieval in Sparse Aperture Systems with Phase Diversity: A Trade Space Study

Brian J. Daniel<sup>a</sup>, Matthew R. Bolcar<sup>b</sup>, John. R. Schott<sup>a</sup>, and James R. Fienup<sup>b</sup>

<sup>a</sup>Rochester Institute of Technology  
Chester. F. Carlson Center for Imaging Science  
Digital Imaging & Remote Sensing Laboratory  
Rochester, NY, USA

<sup>b</sup>University of Rochester  
The Institute of Optics  
Rochester, NY, USA

## ABSTRACT

Sparse-aperture (SA) telescopes are a technology of interest in the field of remote sensing. Significant optical resolution can be achieved by an array of sub-apertures, mitigating size and weight limitations of full aperture space-deployed sensors. Much of the analysis to date has been done with the assumption that an extended scene is spectrally flat and each pixel has the same spectrum (gray-world assumption). Previous work<sup>1,2</sup> has found the gray-world assumption is not valid when imaging a spectrally diverse scene and/or when the optical configuration is heavily aberrated. Broadband phase diversity (BPD) is an image-based method to detect the aberrations of a system.<sup>3,4</sup> It also assumes a gray-world. Digital simulations that quantify the limitations of BPD with respect to spectral diversity of the extended scene, the RMS of the optical path difference (OPD), noise of the system, and band width of the sensor are presented.

**Keywords:** Sparse apertures, phase diversity, phase retrieval, gray-world assumption, remote sensing

## 1. INTRODUCTION

The Hubble Space Telescope, with a 2.4m diameter primary mirror, is the maximum cargo load of current deployment vehicles.<sup>5</sup> Some options to mitigate the launch vehicle limitations are to use light-weight optics that unfold post-launch, or to create a system that can be assembled with multiple launch missions. Therefore, sparse and segmented apertures are the focus of this research. A sparse aperture telescope has an aperture area that is much less than the encircling area of the total array. The two methods of obtaining such a system are the multiple-telescope array and a common secondary array. The latter splits up the primary mirror into subapertures with a common secondary mirror, and the former is an array of telescopes all phased to image on the same focal plane. Regardless of the method, misalignments in the subapertures are extremely detrimental to the restored image quality. The second piece of this effort (not presented here) will examine the characterization of misalignment errors with an image chain approach.

The method of phase diversity was developed in 1977 in order to detect the wavefront aberrations in a monochromatic system.<sup>6</sup> Utilizing multiple images of the same object with different amounts of defocus, the misalignment errors can be estimated. Some variations of phase diversity include adding piston to multiple subapertures to introduce diversity<sup>7</sup> and applying phase diversity to broadband images.<sup>4</sup>

---

Further author information: (Send correspondence to B.J.D.)  
B.J.D.: E-mail: bjd0126@cis.rit.edu

## 2. BACKGROUND

### 2.1 Sparse Aperture Model & Image Generator

A sparse aperture pupil function can be written in terms of its subapertures, given as

$$p(x, y; \lambda) = \sum_{n=1}^P p_n(x, y; \lambda) = \sum_{n=1}^P |p_n(x, y; \lambda)| e^{i w_n(x, y; \lambda)} \quad (1)$$

where  $n$  is the index of each subaperture,  $w_n$  is the phase caused by optical aberrations for each subaperture, and  $|p_n(x, y; \lambda)|$  is the amplitude transmittance. The phase is related to the distance the wavefront deviated from the ideal sphere caused by the less than ideal optics. This optical path difference (OPD) is related to the phase by Eqn. (2).

$$w_n(x, y; \lambda) = \frac{2\pi}{\lambda} OPD_n(x, y) \quad (2)$$

The OPD can be modeled as a summation of orthonormal polynomials. Zernike polynomials are commonly used. The first order Zernikes relate to piston, tip and tilt misalignments for each subaperture. First order aberrations dominate the OPD because subapertures rely on physical mechanics for alignment to within  $\lambda/10$ , the typical error threshold for optical fabrication. For a bandpass centered in the visible regime in a optical limited system, subapertures need to be aligned to within tens of nanometers, which is extremely difficult. The first order OPD is written in polar coordinates as

$$\begin{aligned} OPD_n(r, \theta) &= \alpha_{1n} \cdot p_n(r, \theta) + \alpha_{2n} r \cos \theta \cdot p_n(r, \theta) + \alpha_{3n} r \sin \theta \cdot p_n(r, \theta) \\ &= \sum_i \alpha_{in} \phi_{in}(r, \theta) \end{aligned} \quad (3)$$

where  $\phi_{in}$  are basis functions for piston, tip and tilt, illustrated in Figure 1. The propagation of light through

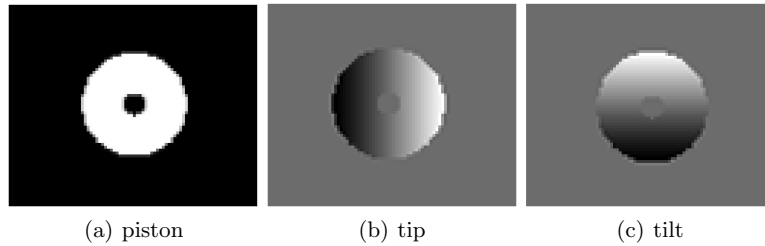


Figure 1. First order Zernike polynomials

this system is based on linear systems theory.<sup>8</sup>

We assume our sparse aperture system is in a remote sensing application, where light reflected from the object is incoherent. The intensity is then assumed to be Linear and Shift Invariant (LSI), so the image equation for a panchromatic system is then

$$g(x, y) = \int r(\lambda) f(x, y; \lambda) * h(x, y; \lambda) d\lambda + n(x, y) \quad (4)$$

$$= \iiint r(\lambda) f(x', y'; \lambda) h(x - x', y - y'; \lambda) dx' dy' d\lambda + n(x, y) \quad (5)$$

where  $r(\lambda)$  is the spectral response of the sensor at wavelength  $\lambda$ ,  $f(x, y; \lambda)$  is the object scene with the spectral nature explicitly stated,  $n(x, y)$  is the additive noise of the system assuming it has the same random properties for all wavelengths,  $g(x, y)$  is the image at the focal plane, and  $h(x, y; \lambda)$  is the point spread function (PSF) of the system at band  $\lambda$ . The  $*$  indicates the continuous convolution operation. Using the filter theorem, the spatial frequency domain expression equivalent to Eqn. 4 is

$$G(\xi, \eta) = \int r(\lambda) F(\xi, \eta; \lambda) \cdot \mathcal{H}(\xi, \eta; \lambda) d\lambda + N(\xi, \eta), \quad (6)$$

where  $\xi$  and  $\eta$  are the  $x$  and  $y$  spatial frequency coordinates, and the capital letters are the fourier transform pairs of the associated lower case letters. The normalized Optical Transfer Function (OTF) is the fourier transform pair of the PSF, given in terms of the pupil function ( $p$ ) for an instrument with focal length  $f$  as

$$\mathcal{H}(\xi, \eta; \lambda) = \frac{p(-\lambda f \xi, -\lambda f \eta; \lambda) \star p(-\lambda f \xi, -\lambda f \eta; \lambda)}{\int \int_{-\infty}^{+\infty} p(-\lambda f \xi, -\lambda f \eta; \lambda) d\xi d\eta}. \quad (7)$$

The OTF is the autocorrelation of the scaled pupil function. This method is used to simulate the input imagery for broadband phase diversity (BPD).

## 2.2 Broadband Phase Diversity

The method of broadband phase diversity estimates the phase of the pupil function and the object concurrently by using multiple panchromatic images, each with known phase differences. For example, with the introduction of two beam splitters and two more detector arrays that are a known distance away from the focal plane, a remote sensing imaging system can simultaneously capture three images, each with different defocus. The generalized discrete imaging equation for that system is<sup>6</sup>

$$g_k(x, y) = \sum_{\lambda \in \Lambda_k} \sum_{x', y' \in \chi} r(\lambda) f(x', y'; \lambda) h_k(x - x', y - y'; \lambda) + n(x, y), \quad (8)$$

where the subscript  $k$  indicates the diversity channel, each discrete wavelength  $\lambda$  is contained in the set,

$$\Lambda_k = \{\lambda_{k0}, \lambda_{k1}, \dots, \lambda_{kL_k}\}, \quad (9)$$

and  $\chi$  is the set of spatial coordinates given as,

$$\chi = \left\{ -\frac{N}{2}, -\frac{N}{2} + 1, \dots, \frac{N}{2} - 1 \right\} \times \left\{ -\frac{N}{2}, -\frac{N}{2} + 1, \dots, \frac{N}{2} - 1 \right\}. \quad (10)$$

The phase difference between the  $k$  channels is written explicitly as

$$p_k(x, y; \lambda) = \left[ \sum_{n=1}^P |p_n(x, y; \lambda)| e^{i w_n(x, y; \lambda)} \right] e^{i \theta_k(x, y; \lambda)}, \quad (11)$$

where  $\theta_k$  is a phase added to the entire pupil function, as opposed to individual subapertures.

A necessary assumption that is the foundation of this algorithm and is the focus of this work will now be made. If we assume the spatial component of the object is separate of the spectral component,<sup>4</sup> we can say

$$f(x, y; \lambda) \approx f_A(x, y) f_\Lambda(\lambda). \quad (12)$$

Eqn. 12 essentially states that at each pixel we have the same spectrum. An equivalent statement is that the world is assumed to be gray. Since this is clearly not true for earth observing remote sensing, the dependency of the robustness of BPD on this assumption is the focus of this work. Because of the separability of the object in the assumption, we can rewrite Eqn. 8 as

$$g_k(x, y) = \sum_{x', y' \in \chi} f_A(x', y') \sum_{\lambda \in \Lambda_k} [r_k(\lambda) f_\Lambda(\lambda)] h_k(x - x', y - y'; \lambda) + n(x, y) \quad (13)$$

$$= \sum_{x', y' \in \chi} f_A(x', y') \left[ \sum_{l=0}^{L_k} T_{kl} h_k(x - x', y - y'; \lambda) \right] + n(x, y) \quad (14)$$

$$= f_A(x, y) \star h_k^b(x, y) + n(x, y), \quad (15)$$

where the monochromatic PSF weighting that incorporates the object and system spectral characteristics is

$$T_{kl} = r_k(\lambda_{kl}) f_\Lambda(\lambda_{kl}), \quad (16)$$

and the broadband PSF is explicitly defined as

$$h_k^b(x, y) \equiv \sum_{l=1}^{L_k} T_{kl} h_{kl}(x, y; \lambda_{kl}). \quad (17)$$

Eqn. 17 is just a weighted sum of monochromatic PSFs. Using this formulation we can write the broadband imaging equation in the same form as the monochromatic imaging equation. Utilizing the maximum likelihood formulation from previous work, assuming the noise is gaussian distributed, the maximum likelihood for broadband estimation is<sup>4</sup>

$$L_G(\alpha) = \sum_{\xi, \eta=0}^{N-1} \frac{|\sum_{k=1}^K G_k(\xi, \eta) \hat{\mathcal{H}}_k^{b*}(\xi, \eta)|^2}{\sum_{k=1}^K |\hat{\mathcal{H}}_k^b(\xi, \eta)|^2}, \quad (18)$$

where  $\hat{\mathcal{H}}_k^b$  is the broadband OTF based on the estimated values for  $\alpha$ , which make up the phase of the pupil function. Finding the set of  $\alpha$  that maximizes the likelihood equation is equivalent to finding the set of  $\alpha$  that minimizes the negative of the likelihood, shown here as

$$E(\alpha) = - \sum_{\xi, \eta=0}^{N-1} \frac{|\sum_{k=1}^K G_k(\xi, \eta) \hat{\mathcal{H}}_k^{b*}(\xi, \eta)|^2}{\sum_{k=1}^K |\hat{\mathcal{H}}_k^b(\xi, \eta)|^2}. \quad (19)$$

A common method of minimization of Eqn. 19 is a *quasi*-Newton method featuring Broyen-Fletcher-Goldgarb-Shanno (BFGS) update of the Hessian.<sup>9</sup> The method belongs to a broad subclass of minimization techniques termed Gradient Methods. These methods work most efficiently when the analytical gradient is supplied. The analytical gradient of Eqn. 19 is derived and reported in previous publications<sup>4</sup> and is used in the implementation for this work. It's important to note that *quasi*-Newton method works with a limited number of unknowns. If one were to want a point-by-point phase estimate, another minimization routine should be used.

### 3. APPROACH

The purpose of the simulations described in this section is to build a trade space of all the factors that stress the gray-world assumption of Eqn. 12. Figure 2 illustrates the parameters that are expected to affect the performance of BPD. The spectral 'grayness' of a scene is related to the spectral nature of the world that we

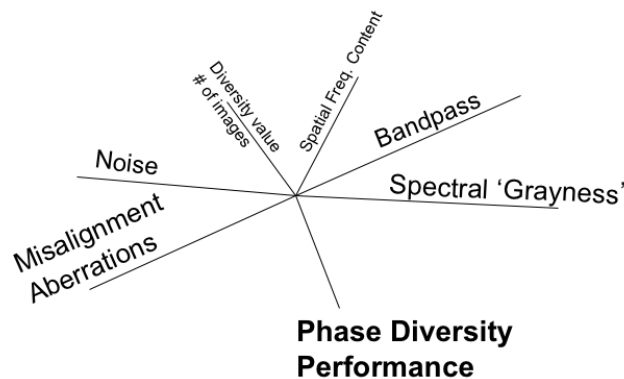


Figure 2. Sketch of the trade space for a phase diversity sparse aperture system.

observe. The spectral nature of a forest is very different from the spectral nature of a city. In order to simulate this effect, we use real hyperspectral data as the object for our model.

Hyperion is a sensor on board NASA's EO1 satellite.<sup>10</sup> With a GSD of 30 m, Hyperion has a coarse spatial resolution compared to an actual SA system flying in low earth orbit ( $\sim 1$  m GSD), but it has 242 spectral bands from the ultraviolet to long-wave infrared. A 3 channel RGB image of a portion of the flight line is shown in Figure 3. Fifty bands are of interest, from 0.42 - 0.92  $\mu\text{m}$  with a 0.01  $\mu\text{m}$  spectral sampling distance. The

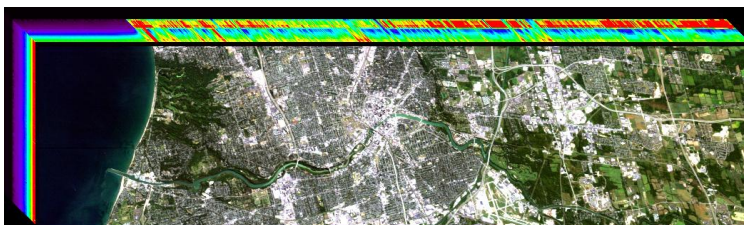


Figure 3. A portion of the Hyperion data set. The flight line transverse Lake Ontario into Western New York. (North to left)

spectral content is appealing because of the differences in land cover it transverse. The north end of the flight line is over water and the coast. As the line travels south it covers a city center (Rochester) and continues south to more rural landscapes. The band width of this data is a degree of freedom in our trade space (see Figure 2). The hyperspectral data set is divided up into 16 subsets of dimensions 200 pixels  $\times$  200 pixels  $\times$  # of bands.

Misalignment aberrations are another factor that affect the validity of the gray world model. Work investigating the forward model for an SA system concluded that highly aberrated optics introduced spectral artifacts in the restored imagery that aren't there when modeled with the gray world assumption.<sup>2</sup> Therefore, misalignment aberration is a degree of freedom in our trade space, measured as the RMS of the OPD.

The width of the bandpass has a major influence on BPD performance. Because the fill factor of SA systems is so low ( $\sim 17\%$ ), opening the bandpass as wide as possible is imperative to the signal-to-noise ratio (SNR). The trade-off of bandpass width versus noise and any dependency on the spectral nature of the scene and misalignment errors is investigated with these simulations.

Other parameters that affect BPD performance include how many channels, or how many diversity images we use as input data. In order to be consistent throughout the simulations, we will use 3 images with (-2, 0, +2) waves of defocus at the edge of the pupil function. The spatial frequency content of the imagery is a parameter that is impossible to control in the field, but we will vary it by using different subsets of imagery. It would be difficult for BPD to find a reasonable OPD estimate when imaging over water, or some other spatially homogeneous area. One subset of the Hyperion data taken over Lake Ontario will be used to observe the effect of spatial frequency (or lack thereof) on BPD.

The triarm-9 SA configuration is the pupil function array that was studied, shown in Figure 4. That, and the other parameters that were modeled are shown in Table 1.

Parameter	Value(s)
SA Configuration	Triarm-9
Radiance Data Subsets	Hyperion (200 pixels $\times$ 200 pixels $\times$ #bands)
Bandpasses	single band 0.55, 0.5-0.6, 0.4-0.7, & 0.4-0.9 $\mu\text{m}$
SNR	10, 100, & 1000
RMS of aberration	0.1, 0.3, 0.5, 0.7, 0.9, & 1.0 waves at $\lambda_0$
Number of diversity images	3
Amount of defocus diversity	$\pm 2$ waves at $\lambda_0$

Table 1. Simulation parameters for building trade-space.

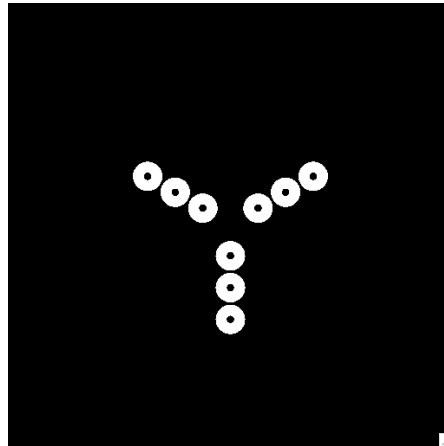


Figure 4. Triarm-9 sparse aperture pupil function used in the simulations presented here.

### 3.1 Performance Evaluation

BPD solves for the aberration coefficients of the polynomials that make up the phase of the pupil function. When we try to quantify the performance of phase diversity, it would make sense to compare the modeled phase coefficients with that of the estimated. However, within the minimization process of phase diversity, the coefficients that are estimated can have an introduced global piston, tip, or tilt error, illustrated in Figure 5. These global terms cause only an image shift, and therefore, do not negatively affect the performance of the

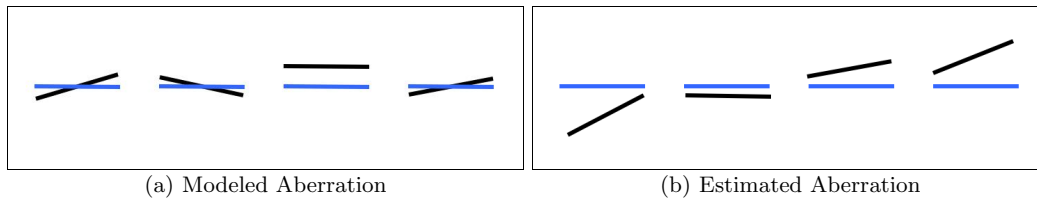


Figure 5. The introduction of a global tilt can make the coefficients for each subaperture parameter meaningless. The evaluation of phase diversity performance must take this into account.

system. In order to correctly evaluate phase diversity, we must take this into account. The following describes two methods used to evaluate BPD.

Using the estimated phase coefficients output by phase diversity, we can generate a phase map of the pupil function. We project the phase maps onto the global piston, tip and tilt basis functions. The global basis functions for a simple three aperture array are shown in Figure 6. The global piston, tip, and tilt aberrations are

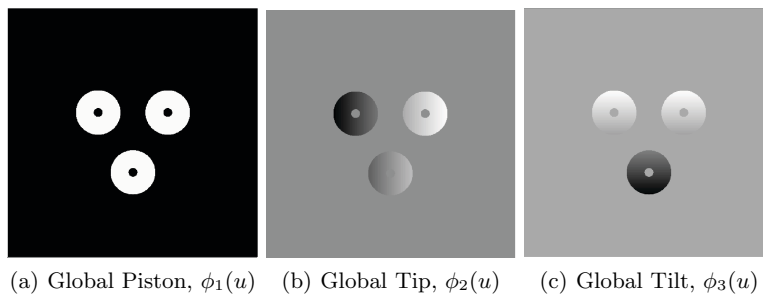


Figure 6. Global variables the estimate and modeled phase maps are projected on in order to remove the global piston, tip and tilt introduced in phase diversity. In this case, the aperture is a Tri configuration.

then removed from both the estimated phase map and the modeled phase map. The de-globalized phase maps are compared using root-mean-squared error (RMSE), shown in Eqn. 20.

$$RMSE_{dg} = \sqrt{\frac{1}{N} \sum_u [OPD_{dgM}(x, y) - OPD_{dgE}(x, y)]^2} \quad (20)$$

The subscript *dg* refers to the quantity being de-globalized, the de-globalized optical path difference for the modeled pupil function is  $OPD_{dgM}$  and  $OPD_{dgE}$  is the de-globalized optical path difference estimated by phase diversity. This method is referred to as De-globalized RMSE, or DGRMSE for short.

The second method of evaluation for phase diversity is the *residual strehl ratio*. We start with a pupil function created from the difference OPD, defined as

$$p_{diff}(x, y) = |p(x, y)| e^{\frac{2\pi i}{\lambda} [OPD_{mod}(x, y) - OPD_{est}(x, y)]} \quad (21)$$

where  $|p(x, y)|$  is the amplitude mask of the modeled pupil,  $OPD_{mod}$  is the modeled OPD, and  $OPD_{est}$  is the BPD estimated OPD. The point-spread function (PSF) of the difference pupil and an unaberrated pupil function are calculated as the inverse fourier transform of Eqn. 7. The residual strehl ratio compares the center lobe of the difference PSF with that of the unaberrated PSF, shown in Eqn. 22.

$$Strehl_{res} = \frac{PSF_{diff}(x_{lobe})}{PSF_{unab}(x'_{lobe})} \quad (22)$$

Both  $x_{lobe}$  and  $x'_{lobe}$  are two dimensional position vectors where the associated PSF is centered. With only global misalignment error, the PSF is just shifted in the tip/tilt case. The value of the PSF at the center lobe isn't much different than an unaberrated PSF, giving a Strehl ratio of approximately 1. Subtracting the estimated phase map from the modeled phase produces a phase map of the global misalignments,  $PSF_{diff}$ , provided we have a good phase estimate. Significant deviation of the Strehl from the value of 1 is due to failure in the algorithm to correctly estimate the phase.

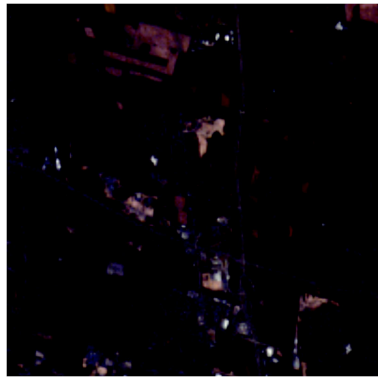
The Strehl ratio and De-globalized RMSE are used as an evaluation tool for the performance of the BPD algorithm.

#### 4. RESULTS & OBSERVATIONS

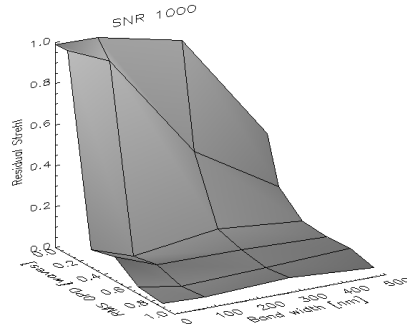
The simulated parameters of Table 1 provided a coarse sampling of the total trade space. Figures 7, 9, and 10 are selected results of the residual strehl ratio calculated on the BPD results for three of the sixteen Hyperion subsets.

What looks like a shelf in the upper left hand corner of the residual strehl plots is where BPD finds the OPD almost exactly, where residual strehl has a value close to 1. In de-globalized RMSE plots, a value close to 0 is successful. Please note, the x-axis on DGRMSE plots are opposite those of residual strehl plots. DGRMSE tells a similar story to the residual strehl, so we only show DGRMSE results for one selection, shown in Figure 8. We are focusing on the fall off in performance with respect to aberration, band width, and noise.

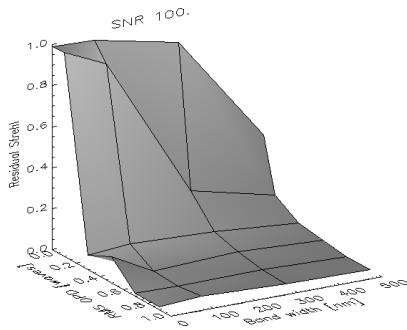
The failure of BPD usually occurs due to the minimization routine getting caught in a local minimum, or when the global minimum is too hard to find. The *capture range* is defined as the region in the metric space where the global minimum can be found. By using multiple starting conditions, we get a sense of the size of the capture range in certain physical situations. The most obvious observation of all 3 sets is the degradation in performance with SNR. For most cases, as expected, 1000 SNR images out performed 100 SNR situations. The capture range is larger for less noise. Note that for Figure 10, there is little change between 1000 and 100 SNR. This phenomenon will be discussed momentarily. The OPD drastically affects BPD performance. Most image subsets have an extreme fall off in performance at or below 0.3 waves RMS OPD. A third to a quarter wave of aberrations is significant in that the capture range becomes too small to find the global minimum. For most cases, BPD was successful at these ranges, but not always. A possible method for extending the capture range is to use the average spectrum of the object, which is equivalent in having a full-field 1-pixel spectrometer



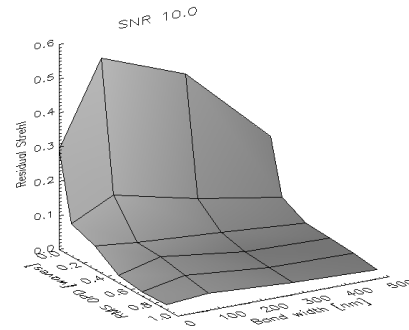
(a) RGB Image



(b) 1000 SNR



(c) 100 SNR



(d) 10 SNR

Figure 7. Surface plots of the residual strehl ratio (Eqn. 22) versus RMS of the OPD (aberration) on the x axis, band width on the y-axis for a rural/small town subset of Hyperion

on board the air/space craft. This was not attempted for the results presented here, rather the value for the gray-world spectrum ( $T_{kl}$ ) was uniform for these runs (e.i. the initial spectrum was all ones).

The affects of the band width show in all cases, that 500 nm is too large for effective BPD. With a band width of 500 nm, performance depends on the spectral nature of the scene. The rural/small town scenes and the city scenes seem to perform fairly well. When imaging a forest, or high amounts of vegetation, 500 nm proves to be too much for BPD. This is most likely due to the spectral nature of vegetation. Chlorophyll's spectrum has a steep jump around 750 nm. The 500 nm bandpass was the only bandpass that captures this phenomenon. Future work will investigate further.

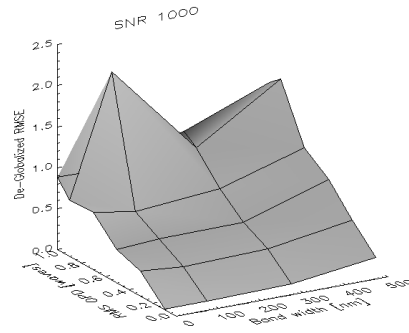
## 5. FUTURE WORK

There is much more work to be done. Some of the effects observed could be dependent on the Hyperion data set. Future work will be to use this methodology on other data sets from different sensors, such as HyMap and Hydice. Also, other pupil configurations will be tested. The Golay-6 aperture is of special interest.

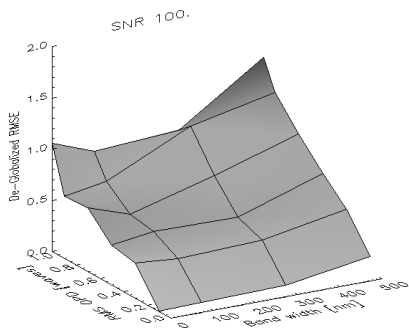
In future work the average spectrum of the hyperspectral input will be used as  $T_{kl}(\lambda)$ . This should extend the capture range. Finer sampling in the OPD around 0.3 waves RMS will be done. The 10 SNR case proved to be unrealistically optimistic, so sampling the trade-space starting at 50 SNR seems appropriate. There are many cases where SNR of 100 is similar to the results of 1000 SNR (Figure 9), so those cases are where the performance is limited by other parameters. The band widths will be sampled from 100 to 400 nm with finer detail, and with a shifted bandpass center to study the affects of the vegetation spectrum.



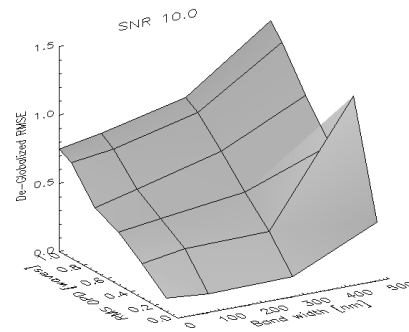
(a) RGB Image



(b) 1000 SNR



(c) 100 SNR



(d) 10 SNR

Figure 8. Surface plots of the de-globalized RMSE (Eqn. 20) versus RMS of the OPD (aberration) on the x axis, band width on the y-axis for a rural/small town subset of Hyperion

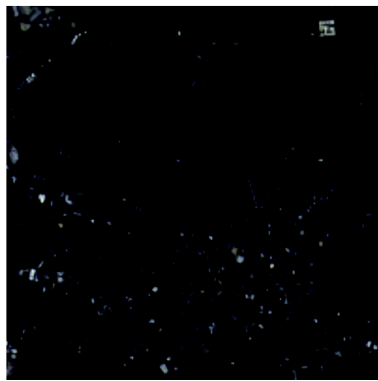
Work will be done to quantify the spectral nature of the hyperspectral input images. Statistical models and geometric interpretations will be used. We hope to be able to quantify and identify the spectral character of the object that would cause the capture range of the metric space to decrease in size.

### ACKNOWLEDGMENTS

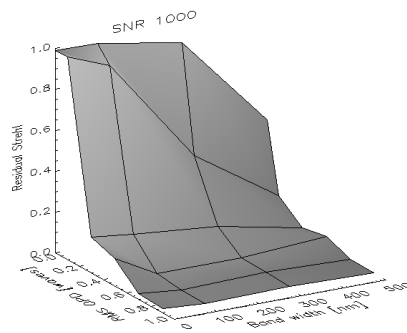
Many thanks are owed to Dr. David Messinger and Dr. Rolando Raqueno, for without their contributions, this work was not possible.

## REFERENCES

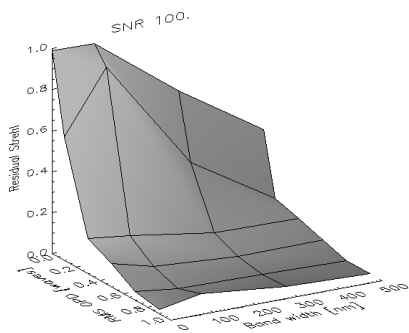
1. R. E. Introne, *Enhanced Spectral Modeling of Sparse Aperture Imaging Systems*. PhD thesis, Rochester Institute of Technology, 2004.
2. N. Block, "A sensitivity study of a polychromatic sparse-aperture system," Master's thesis, Rochester Institute of Technology, 2005.
3. R. G. Paxman, T. J. Schultz, and J. R. Fienup, "Joint estimation of object and aberrations by using phase diversity," *J. Opt. Soc. Am.* **9**, pp. 1072–1085, July 1992.
4. J. H. Seldin, R. G. Paxman, V. G. Zarifis, L. Benson, and R. E. Stone, "Close-loop wavefront sensing for a sparse-aperture, multiple-telescope array using broad-band phase diversity," in *Imaging Technology and Telescopes*, J. W. Bilbro, J. B. Breckinridge, R. A. Carreras, S. R. Czyzak, M. J. Eckard, R. D. Fiete, and P. S. Idell, eds., **4091**, SPIE Press, 2000.
5. E. J. Chaisson, *The Hubble Wars*, Harper Collins, 1994.
6. R. A. Gonsalves, "Phase retrieval and diversity in adaptive optics," *Optical Engineering* **21**(5), pp. 829–832, 1982.
7. M. R. Bolcar and J. R. Fienup, "Method of phase diversity in multi-aperture systems utilizing individual sub-aperture control," *Unconventional Imaging, Proceedings*, pp. 126–133, August 2005.
8. J. W. Goodman, *Introduction to Fourier Optics*, Roberts & Company Publishers, 2005.
9. J. E. Dennis, Jr. and R. B. Schnabel, *Numerical Methods for Unconstrained Optimization and Nonlinear Equations*, Society for Industrial and Applied Mathematics, 1983.
10. R. Beck, *EO-1 User Guide v. 2.3*. Department of Geography, University of Cincinnati, Cincinnati, Ohio, 45221, 2.3 ed., July 2003.



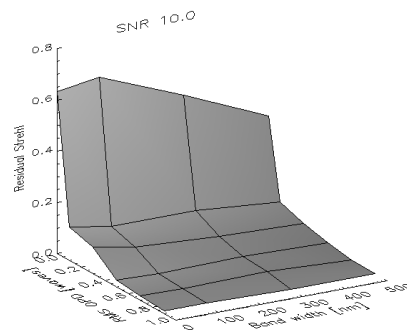
(a) RGB Image



(b) 1000 SNR

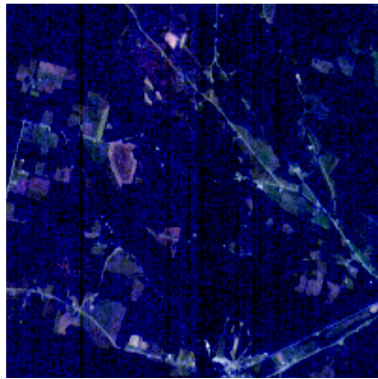


(c) 100 SNR

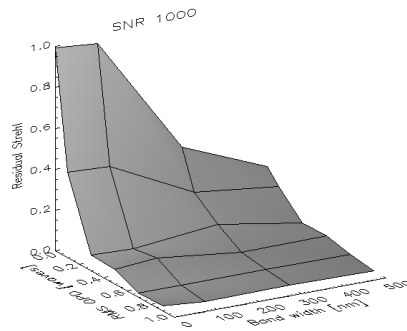


(d) 10 SNR

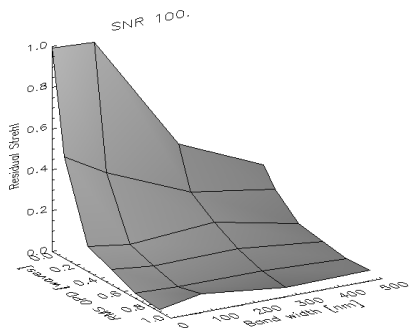
Figure 9. Surface plots of the residual strehl ratio (Eqn. 22) versus RMS of the OPD (aberration) on the x axis, band width on the y-axis for a city center subset of Hyperion



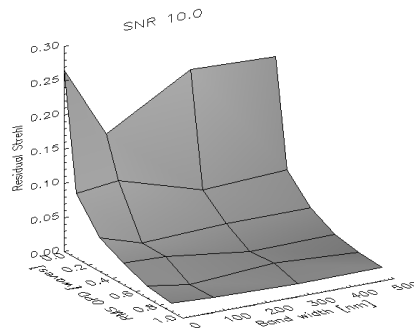
(a) RGB Image



(b) 1000 SNR



(c) 100 SNR



(d) 10 SNR

Figure 10. Surface plots of the residual strehl ratio (Eqn. 22) versus RMS of the OPD (aberration) on the x axis, band width on the y-axis for vegetation subset of Hyperion